Scripta Materialia 115 (2016) 113–117

Contents lists available at ScienceDirect

Scripta Materialia

journal homepage: www.elsevier.com/locate/scriptamat

Regular Article

# Grain boundary engineering of Co–Ni–Al, Cu–Zn–Al, and Cu–Al–Ni shape memory alloys by intergranular precipitation of a ductile solid solution phase

Rebecca D. Dar, Haoxue Yan, Ying Chen *

*Department of Materials Science and Engineering, Rensselaer Polytechnic Institute, 110 8th Street, Troy, NY 12180, USA*

ARTICLE INFO

*Article history:*
Received 12 November 2015
Received in revised form 5 January 2016
Accepted 8 January 2016
Available online 25 January 2016

*Keywords:*
Shape Memory Alloys (SMA)
Grain Boundary Engineering
Precipitation
Ductility
Martensitic phase transformation

ABSTRACT

Many polycrystalline shape memory alloys, e.g., Co–Ni–Al, Cu–Zn–Al, and Cu–Al–Ni, undergo intergranular fracture. To improve their transformation ductility, we perform Grain Boundary Engineering and stimulate the precipitation of a ductile second phase, which is a face-centered-cubic solid solution, along grain boundaries, by tailoring composition and thermal processing. Orientation imaging confirms precipitation along grain boundaries and unimpeded martensite growth toward grain boundary precipitates. Differential Scanning Calorimetry confirms reversible martensitic transformations in these dual-phase samples. These precipitates can accommodate transformation strain, relieve constraint in adjacent austenite grains, and arrest cracks by extensive plastic deformation, thereby improving transformation ductility and shape memory effects.



Shape Memory Alloys (SMAs), due to their ability to undergo reversible martensitic transformations and recover large strains, are promising for many applications such as actuation [1,2], energy conversion [3,4], damping [1,5], and sensing [6,7]. Ni–Ti SMAs are known for their excellent shape memory properties and transformation ductility even in polycrystalline forms (possibly due to their particular transformation crystallography and grain texture [8]), but they are relatively expensive and have only moderate fatigue properties [9]. Many other SMAs, such as Cu–Zn–Al [10,11], Cu–Al–Ni [12], Co–Ni–Al [13–15], Co–Ni–Ga [16], and Ni–Mn–Ga [17], have excellent shape memory properties when they are single crystalline. However, they are typically brittle and prone to intergranular fracture in polycrystalline forms. The transformation shear occurs in different directions in different grains during stress-induced martensitic transformation, resulting in stress concentration at grain boundaries and subsequently fracture along them.

Efforts have been attempted for improving the ductility of these polycrystalline SMAs and typically involve manipulating the grain size. For example, grain refinement, achieved by adding elements such as Zr, Ti, B, V, Cr [18], Gd [19], has been utilized in polycrystalline SMAs such as Ni–Mn–Ga [19], Cu–Zn–Al [18,20], Cu–Al–Ni [21], and Cu–Al–Ni–Ti [22], as finer grains provide better strain accommodation (for example, they alter the fracture mode from intergranular to mostly ductile transgranular during fracture impact test [18,21]). On the other hand, excellent shape memory and transformation ductility have been achieved in oligocrystalline SMAs such as bamboo-grain-structured microwires [23–25], where triple junctions are eliminated, grain boundary area is minimized, and surface relaxation is significant, reducing strain incompatibility at grain boundaries [26]. However, for both oligocrystalline and bulk polycrystalline SMAs, it is still highly desirable and in many cases necessary to increase the resistance to fracture in grain boundary regions during stress-induced transformations for practical use.

In this paper, we demonstrate a Grain Boundary Engineering (GBE) approach for several typical brittle polycrystalline SMAs, including Co–Ni–Al, Cu–Zn–Al, and Cu–Al–Ni systems, which have different crystallographic transformation pathways and thermomechanical properties. Moreover, Co–Ni–Al and Cu–Al–Ni are promising inexpensive candidates for high temperature SMAs. In the phase diagrams for these and many other SMA systems (see Fig. 2), the austenite regime is bordered by a dual-phase regime comprised of austenite and a solid solution phase with a Face-Centered-Cubic (FCC) crystal structure. The present GBE approach involves precipitation of a thin layer of the non-transforming, ductile FCC solid solution phase along grain boundaries in the austenite phase, as illustrated in Fig. 1(b). Compared to GBE methods that involve thermomechanical processing [27], the present *grain boundary phase engineering* approach is straightforward to implement and is scalable at a low cost. It is applicable to bulk polycrystals as well as wires, ribbons and sheets, and porous SMAs.

The addition of an FCC solid solution second phase to extremely brittle single-phase polycrystalline SMAs has been found to significantly improve ductility [28–32]. This is evident in Fig. 1(e) and (f), which

* Corresponding author.
*E-mail address:* cheny20@rpi.edu (Y. Chen).

http://dx.doi.org/10.1016/j.scriptamat.2016.01.014
1359-6462/

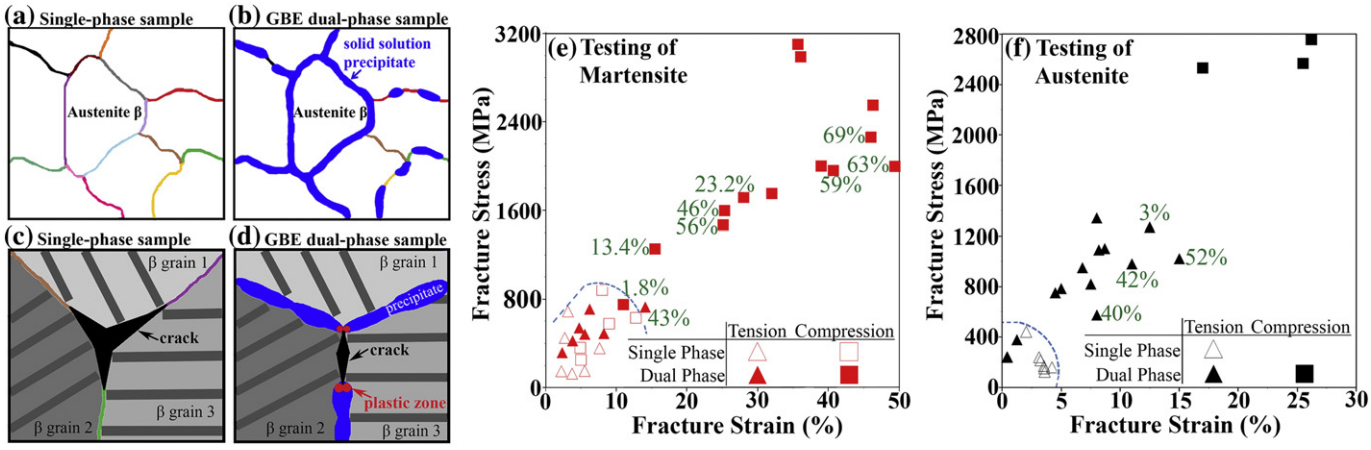


**Fig. 1.** (Color online) Schematic comparisons between single-phase SMAs (a, c) and grain boundary engineered (GBE) dual-phase samples where a thin layer of an FCC solid solution phase (in blue) precipitates along grain boundaries (b, d). During formation of martensite (in dark gray), cracks may propagate along grain boundaries in single-phase samples (c), but may be arrested by ductile precipitates at grain boundaries (d). Literature results for polycrystalline SMAs initially in martensitic and austenitic state are assembled in (e) and (f), respectively. Single phase data (open symbols) are enclosed by dashed blue lines, and include Cu–Al [54], Cu–Al–Ni [33,54–56], Cu–Al–Ni–Ti–Cr [54], Cu–Al–Be–B [57], Co–Ni–Ga [51], and Ni–Mn–Ga [31]. Non-GBE dual-phase data (filled symbols) include Co–Ni–Al [28,32,58], Co–Ni–Ga [51], Ni–Al–Fe [28,35], Ni–Al–Cr [28], Ni–Mn–Ga and Ni–Mn–Fe–Ga [31], Ni–Mn–Cu–Ga [59], Ni–Mn–Co–Ga [60], Ni–Mn–Fe–In [61], and Fe–Mn–Al–Ni [29]. The FCC solid-solution second-phase fraction, if known, is also provided.

summarize literature data for fracture stress and fracture strain of polycrystalline SMAs initially in martensitic and austenitic state, respectively. In Fig. 1(e–f), data for dual-phase SMAs containing an FCC solid solution phase are shown as filled symbols; there is some spread in data due to different alloys and compositions, testing temperatures (mostly at room temperature) with respect to transformation temperatures, and second phase fractions. When the matrix is initially martensitic, martensite variant reorientation and conversion occurs at low loads [33,34] while at high loads dislocation plasticity might take place [34]. In Fig. 1(e), the fracture strain for single-phase samples was mostly below 10%, but was as high as 50% in dual-phase samples. However, testing SMAs that are initially austenitic and undergo martensitic transformation upon loading beyond a critical stress is more relevant to applications. In most brittle single-phase polycrystalline samples, fracture occurs before the transformation is complete. In Fig. 1(f), the majority of single-phase data is clustered around 2.5–4.5% fracture strain while dual-phase values are mostly 5–30%. However, in these prior studies, the materials are non-GBE dual-phase SMAs, i.e., the precipitation was not intentionally controlled along grain boundaries and a high fraction of precipitates were present throughout the grains. While grain interior precipitates significantly improve alloy ductility, they replace transforming material and may interfere with reversible transformation, reducing the overall recoverable strain and impeding strain recovery. In GBE dual-phase samples as illustrated in Fig. 1(b), however, precipitation of the second phase occurs primarily along grain boundaries. This has an optimal effect on ductility because the second phase can cushion grain boundaries, which are the weak links, as they are stressed [28,35]; the formation of a network of thin intergranular precipitates requires a very small volume fraction of precipitates compared to non-GBE dual-phase materials, minimizing the effect on martensitic transformation inside grains. We tailor alloy composition and thermal treatment sequence, temperature, and duration to promote grain boundary precipitation and control the fraction and morphology of the precipitates in Co–Ni–Al, Cu–Zn–Al, and Cu–Al–Ni polycrystalline SMAs [36].

Cast ingots of $Co_{45.46}Ni_{39.40}Al_{15.14}$ wt.% and $Cu_{70}Zn_{26}Al_4$ wt.% were prepared by arc melting and casting in a copper chill mold in high purity argon and $Cu_{86}Al_{11}Ni_3$ wt.% was purchased from American Elements. These alloy compositions are marked as a red dot in Fig. 2(b), (d), and (f), respectively; they all lie inside the austenite plus solid solution dual-phase regime in each of these isothermal phase diagrams. Thermal treatments were carried out in argon with 1% hydrogen, at relatively high temperatures within the temperature range where two-phase

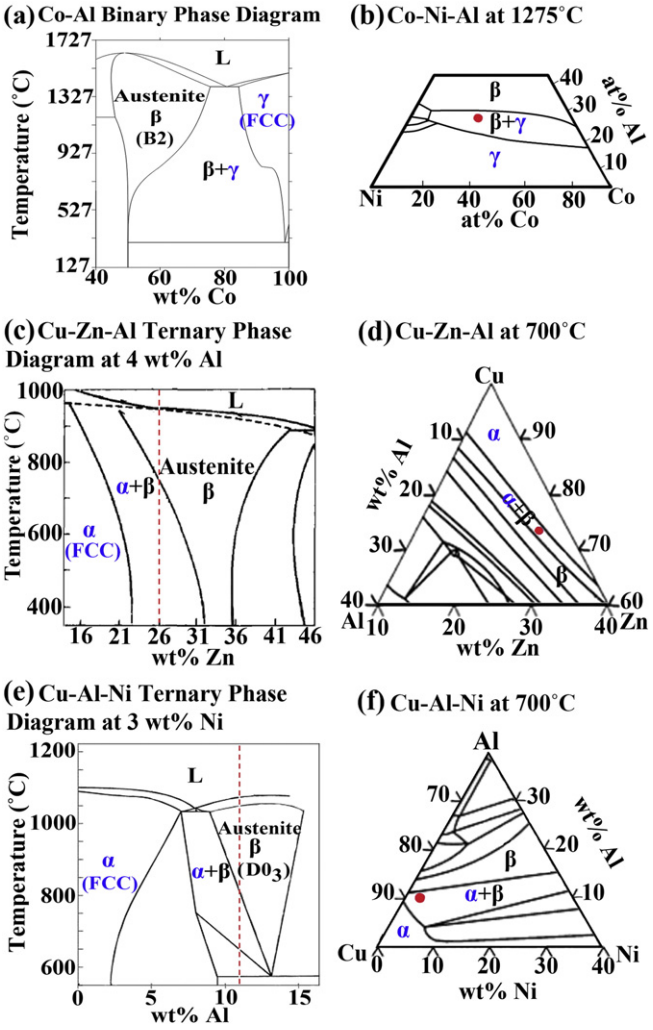


**Fig. 2.** (Color online) (a) Co–Al phase diagram [62]; (b) A Co–Ni–Al isothermal section [30]; (c) Cu–Zn–Al phase diagram at 4 wt.% Al [63] with 26 wt.% Zn shown as a dashed red line; (d) A Cu–Zn–Al isothermal section [64]; (e) Cu–Al–Ni phase diagram at 3 wt.% Ni [41] with 11 wt.% Al shown as a dashed red line; (f) A Cu–Al–Ni isothermal section [64]. The compositions of present alloys are shown as red dots in (b), (d), and (f).

equilibrium exists in order to promote precipitate growth along grain boundaries. Relatively low thermal treatment temperatures lead to nucleation of a large number of precipitates within grains and slow precipitate growth, producing numerous small precipitates inside grains. On the contrary, at higher thermal treatment temperatures, nucleation of the second phase is difficult and usually nuclei preferentially form heterogeneously at grain boundaries, and this also results in less precipitation inside grains. Treatments limited to a few hours or less are more desirable because longer holding periods tend to result in significant precipitate growth and large precipitates, although precipitate continuity is usually also improved as a result. Subsequently, samples were quenched in ice water, mounted in epoxy, and polished. Optical imaging was conducted with a LECO Olympus PMG–3 microscope. Orientation mapping was carried out using a Carl Zeiss Ultra 1540 Scanning Electron Microscope equipped with a NordlysNano Electron Backscatter Diffraction (EBSD) detector. A Differential Scanning Calorimeter (TA instruments DSC–Q100) was used to measure transformation temperatures.

The phase diagram for Co–Al is shown in Fig. 2(a); to the right of the austenite β phase region lies a dual-phase regime where β coexists with an FCC solid solution phase γ. Ni–Al has a quite similar phase diagram, and therefore in the Co–Ni–Al system, the β + γ region encompasses a wide range of temperatures [28,30,37] and compositions, as can be seen in the isothermal phase diagram in Fig. 2(b). Increasing Al content at a given temperature in the dual-phase regime will result in a smaller fraction of γ forming; compositions similar to the one selected for this study yield relatively low γ phase fraction. The microstructures shown in Fig. 3(a–b) result from holding the sample at 1375 °C (single β phase region) for 1.5 h, followed by relatively slow ramping at 0.9–1.1 °C/min to 1275 °C, a dwell period of 0–20 min, and quenching. The minor difference in the ramp down rate and dwell period did not produce a significant difference in the resulting microstructures, although precipitate continuity seems slightly greater in Fig. 3(a) compared to Fig. 3(b). Such heat treatments promoted γ precipitate growth along grain boundaries without significant nucleation of precipitates inside austenite grains. γ formed a nearly continuous layer along many grain boundaries (such as those indicated by the red arrows in Fig. 3(a–b)). Even at grain boundaries where γ precipitates are not continuous (e.g., those indicated by the green arrows in Fig. 3(a–b)), they can still effectively impede intergranular crack propagation and prevent avalanche-like failure.

In the Cu–Zn–Al system, an FCC Cu-based solid solution phase, α, can coexist with austenite β ($D0_3$ [38], B2 [38,39] or $L1_2$ structure depending on composition and thermal processing [40]), as can be seen in a vertical section at 4 wt.% Al of the Cu–Zn–Al phase diagram in Fig. 2(c), where the chosen alloy composition is shown as the red dashed line. For this composition, α and β coexists between ~400–780 °C. The volume fraction of α in equilibrium with β increases with decreasing temperature, and therefore dwell temperatures of 600–700 °C were selected so that a relatively low fraction of α forms during thermal treatment. Fig. 3(c) and (d) show microstructures from samples heat treated at 615 °C and 640 °C for 4–4.5 h, showing semi-continuous or nearly continuous α precipitates forming a layer along grain boundaries. There are fewer small precipitates formed inside grains in Fig. 3(d) as compared to Fig. 3(c) due to the higher heat treatment temperature, and the thickness of precipitates along grain boundaries in Fig. 3(d) is fairly constant.

Cu–Al–Ni alloys with 11–15 wt.% Al and 3–5 wt.% Ni typically exhibit shape memory behavior [41,42]. Fig. 2(e) is a vertical section at 3 wt.% Ni of Cu–Al–Ni phase diagram. The present alloy composition is shown as a red dashed line in Fig. 2(e) and as a red dot in Fig. 2(f), an isothermal phase diagram of Cu–Al–Ni. An FCC solid solution phase, α, is in equilibrium with austenite β from ~575 to 1050 °C, and for the chosen composition, the range reduces to ~650–800 °C. A thermal treatment temperature of 725 °C is chosen as it leads to a relatively small

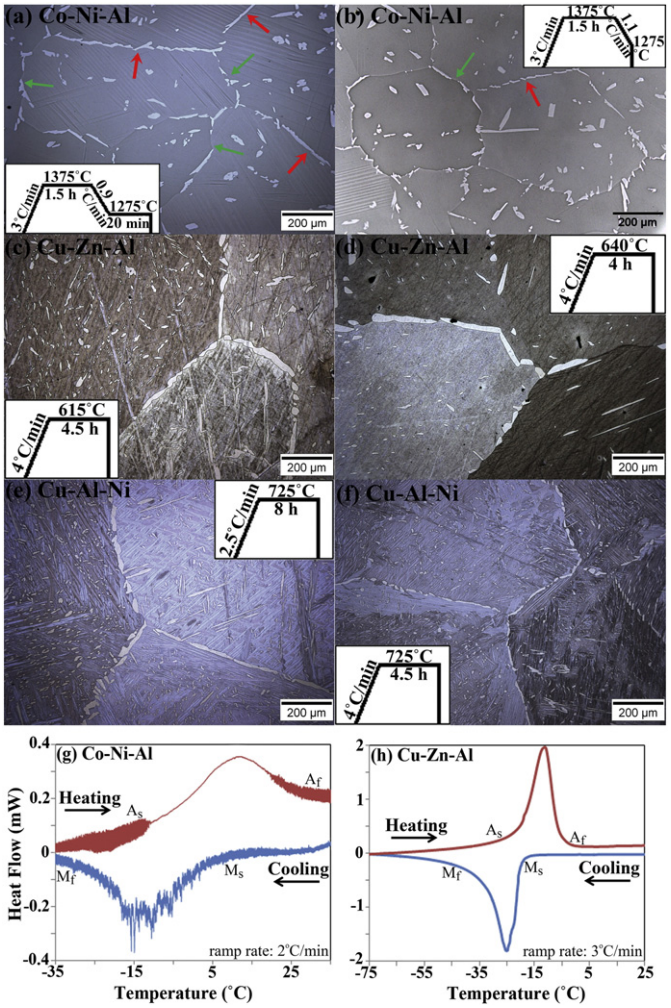


**Fig. 3.** (Color online) (a–b) Co–Ni–Al samples; (c–d) Cu–Zn–Al samples; (e–f) Cu–Al–Ni samples; (g) DSC curve for Co–Ni–Al sample in (a); (h) DSC curve for Cu–Zn–Al sample in (c).

fraction of α but still results in sufficient precipitate nucleation and growth along grain boundaries. A thermal treatment including holding at 725 °C for 8 h resulted in continuous α of even thickness along grain boundaries (Fig. 3(e)). Reducing the dwell period to 4.5 h resulted in considerably smaller (thinner) precipitates everywhere (Fig. 3(f)) than in Fig. 3(e), but the continuity of precipitates along grain boundaries is preserved. Precipitates inside grains in Fig. 3(c–d) seem elongated, and in Fig. 3(e–f), some are needle shaped, possibly due to the high elastic anisotropy of Cu–based alloys [43].

Differential Scanning Calorimetry (DSC) results for GBE samples of Co–Ni–Al (Fig. 3(g)) and Cu–Zn–Al (Fig. 3(h)) reveal reversible martensitic transformations in both samples, as evidenced by peaks in cooling and heating curves. The transformation temperatures for our Cu-Al-Ni alloys are expected to be outside the operating temperature range of the instrument used [44], but martensite needles are visible inside all grains in Fig. 3(e–f). These results suggest that the presence of the non-transforming second phase does not compromise martensitic transformation or the reversibility of the transformation.

Fig. 4 compares crystallographic orientation maps and phase maps for three regions in a Co–Ni–Al sample. This comparison confirms that γ precipitates indeed primarily form along grain boundaries and can stretch continuously for 50–100 μm. In these regions, grain boundaries are found to have general character, and little precipitation has occurred inside grains. In Region 1, shown in Fig. 4(a–b), two different variants of martensite in each grain extend all the way to the grain

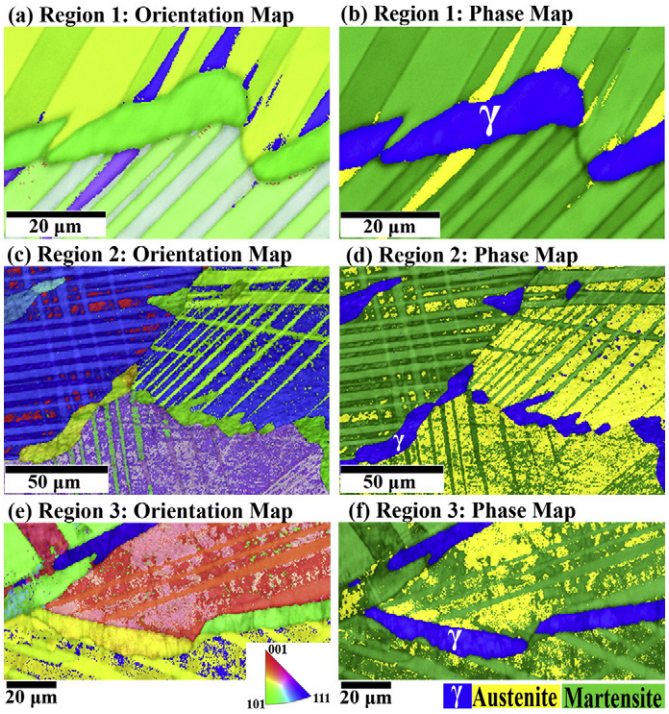


**Fig. 4.** (Color online) (a, c, e) Orientation maps and (b, d, f) the corresponding phase maps (both overlaid with band contrast maps) for three regions in the Co–Ni–Al sample shown in Fig. 3(a). The EBSD scan step size was 0.20, 0.44, and 0.36 μm for regions 1–3 respectively.

boundary, along which oblong, nearly-continuous γ precipitates formed (Fig. 4(b)). It is possible that precipitation of γ particles along grain boundaries and their subsequent growth at the high holding temperature has impeded grain boundary migration during grain growth, leading to the rather curved grain boundary and further hindering intergranular crack propagation. In Region 2 shown in Fig. 4(c–d), the triple junction of three grains shows a partly bare grain boundary and nearly continuous γ precipitates decorating the other two grain boundaries. In Region 3 shown in Fig. 4(e–f), nearly continuous precipitates decorate the horizontal grain boundary, while at the top left a second grain boundary partially decorated with γ is visible. In all regions, martensite plates seem able to remain straight toward γ, which suggests transformation can take place in austenite volume directly adjacent to γ.

In summary, the present GBE approach is promising to drastically improve the transformation ductility of many polycrystalline SMAs. In single-phase polycrystalline SMAs (Fig. 1(a)), bare triple junctions and grain boundaries are prone to crack nucleation and propagation during martensitic transformation due to strain mismatch and stress concentration in these regions. This is illustrated in Fig. 1(c), which shows a crack forming at a triple junction and propagating along adjoining grain boundaries. In the GBE dual-phase samples, however, the FCC solid solution phase (in blue in Fig. 1(b)) precipitated at grain boundaries can accommodate transformation strain in adjacent austenite grains by extensive plastic deformation, relieving local stress concentration and reducing the probability of crack nucleation at grain boundaries. Furthermore, as illustrated in Fig. 1(d), even if an intergranular crack forms, for example, at a bare grain boundary segment, and attempts to grow along a grain boundary, a ductile solid solution precipitate ahead of the crack tip will form a significant plastic zone, effectively increasing the energy barrier for crack growth.

Although it may seem counter-intuitive, in small additions, ductile non-shape-memory precipitates do not impair shape memory effect (SME) or superelasticity [45–52]. Rather, our nanoindentation experiments revealed that austenite regions directly adjacent to precipitates show better strain recovery than austenite regions without precipitates nearby [53]. This is because the second phase plastically accommodates transformation strain. It imposes little constraint on transforming austenite and therefore allows for more extensive transformation due to a lower energy barrier. Precipitates along grain boundaries could alleviate grain boundary constraint and enhance local strain compatibility, lowering the critical stress for transformation and enhancing strain recovery and superelasticity of polycrystalline SMAs. Higher shape recovery is observed in an SMA where precipitates form a thin network along grain boundaries as compared to blocky morphologies of precipitates [45]. Moreover, the strength of polycrystalline SMAs will not be compromised because austenite/precipitate phase boundaries also offer strengthening. Our future work will focus on conducting mechanical tests of GBE samples and optimizing grain boundary precipitation and grain structure simultaneously.

## Acknowledgments

This project is supported by US National Science Foundation with award number DMR #1352524 and RPI start–up funds. EBSD and DSC were conducted using cMDIS and CBIS facilities at RPI, respectively. We would like to acknowledge Ames Laboratory for assistance with preparing Co–Ni–Al and Cu–Zn–Al alloys.

## References

[1] M. Wu, L.M. Schetky, International Conference on Shape Memory and Superelastic Technologies, Pacific Grove, California, 2000 171–182.
[2] K. Ikuta, M. Tsukamoto, S. Hirose, Proceedings of IEEE Robotics and Automation Conference, 1988 427–430.
[3] I. Karaman, B. Basaran, H.E. Karaca, A.I. Karsilayan, Y.I. Chumlyakov, Appl. Phys. Lett. 90 (2007) 172505.
[4] A.L. Browne, P.W. Alexander, N. Mankame, P. Usoro, N.L. Johnson, J. Aase, L. HRL, Smart Materials, Structures, and NDT in Aerospace Conference, Montreal, Quebec, Canada, 2011.
[5] A. Baz, K. Imam, J. McCoy, J. Sound Vib. 140 (1990) 437–456.
[6] K. Ikuta, IEEE International Conference on Robotics and Automation, 1990 2156–2161.
[7] Y. Bellouard, Mater. Sci. Eng. A 481-482 (2008) 582–589.
[8] C.P. Frick, A.M. Ortega, J. Tyber, A.E.M. Maksound, H.J. Maier, Y. Liu, K. Gall, Mater. Sci. Eng. A 405 (2005) 34–49.
[9] S.W. Robertson, A.R. Pelton, R.O. Ritchie, Int. Mater. Rev. 57 (2012) 1–37.
[10] C. Jourdan, J. Gastaldi, V. Roques, G. Grange, S. Belkahla, G. Guenin, Acta Metall. Mater. 43 (1995) 4213–4225.
[11] A. Vivet, C. Lexcellent, J. Phys. IV 9 (1999) 411–418.
[12] Y.H. Lu, L.J. Qiao, W.Y. Chu, Fatigue Fract. Eng. Mater. Struct. 25 (2002) 509–518.
[13] K. Oikawa, L. Wulff, T. Lijima, F. Gejima, T. Ohmori, A. Fujita, K. Fukamichi, R. Kainuma, K. Ishida, Appl. Phys. Lett. 79 (2001) 3290–3292.
[14] B.R. Kanth, N.V. Ramarao, A.K. Panda, R. Gopalan, A. Mitra, P.K. Mukhopadhyay, J. Alloys Compd. 491 (2010) 22–25.
[15] Y. Tanaka, K. Oikawa, Y. Sutou, T. Omori, R. Kainuma, K. Ishida, Mater. Sci. Eng. A 438 (2006) 1054–1060.
[16] Y.X. Li, H.Y. Liu, F.B. Meng, L.Q. Yan, G.D. Liu, X.F. Dai, M. Zhang, Z.H. Liu, J.L. Chen, G.H. Wu, Appl. Phys. Lett. 84 (2004) 51–55.
[17] M. Arndt, M. Griebel, V. Novák, T. Roubíček, P. Šittner, Int. J. Plast. 22 (2006) 1943–1961.
[18] J. Lee, C. Wayman, Metallography 19 (1986) 401–419.
[19] X. Zhang, J. Sui, Z. Yu, W. Cai, J. Alloys Compd. 509 (2011) 8032–8037.
[20] V. Sampath, Mater. Manuf. Process. 21 (2006) 789–795.
[21] J. Lee, C. Wayman, Trans. Jpn. Inst. Metals 27 (1986) 584–591.
[22] K. Sugimoto, K. Kamei, H. Matsumoto, S. Komatsu, K. Akamatsu, T. Sugimoto, J. Phys. Colloq. 43 (1982) 761–766.
[23] S.M. Ueland, Y. Chen, C.A. Schuh, Adv. Funct. Mater. 22 (2012) 2094–2099.
[24] Y. Chen, X. Zhang, D.C. Dunand, C.A. Schuh, Appl. Phys. Lett. 95 (2009) 171906.
[25] Y. Chen, C.A. Schuh, Acta Mater. 59 (2011) 537–553.
[26] D.C. Dunand, P. Müllner, Adv. Mater. 23 (2011) 216–232.
[27] M. Kumar, A.J. Schwartz, W.E. King, Acta Mater. 50 (2002) 2599–2612.
[28] K. Ishida, R. Kainuma, N. Ueno, T. Nishizawa, Metall. Trans. A 22 (1991) 441–446.
[29] M. Vollmer, C. Segel, P. Krooß, J. Günther, L.W. Tseng, I. Karaman, A. Weidner, H. Biermann, T. Niendorf, Scr. Mater. 108 (2015) 23–26.
[30] R. Kainuma, M. Ise, C.C. Jia, H. Ohtani, K. Ishida, Intermetallics 4 (1996) S151–S158.
[31] Y. Xin, Y. Li, L. Chai, H. Xu, Scr. Mater. 57 (2007) 599–601.
[32] Y. Tanaka, T. Ohmori, K. Oikawa, R. Kainuma, K. Ishida, Mater. Trans. 45 (2004) 427–430.
[33] U. Sarı, T. Kırındı, Mater. Charact. 59 (2008) 920–929.
[34] T.W. Duerig, J. Albrecht, G.H. Gessinger, JOM 34 (1982) 14–20.
[35] R. Kainuma, K. Ishida, T. Nishizawa, Metall Trans A 23 (1992) 1147–1153.
[36] Y. Chen, R. Dar, Grain Boundary Engineering of Polycrystalline Shape Memory Alloys by Phase Manipulation for Enhanced Mechanical Ductility and Application Fatigue Life, PCT/US15/59415, 2015.

[37] K. Oikawa, T. Omori, Y. Sutou, R. Kainuma, K. Ishida, J. Phys. IV 112 (2003) 1017–1020.
[38] T. Tadaki, M. Takamori, K. Shimizu, Trans. Jpn. Inst. Metals 28 (1987) 120–128.
[39] S. Miyazaki, K. Otsuka, ISIJ Int. 29 (1989) 353–377.
[40] C. Satto, J. Jansen, C. Lexcellent, D. Schryvers, Solid State Commun. 116 (2000) 273–277.
[41] G. Lojen, I. Anžel, A. Kneissl, A. Križman, E. Unterweger, B. Kosec, M. Bizjak, J. Mater. Process. Technol. 162–163 (2005) 220–229.
[42] R. Dasgupta, J. Mater. Res. 29 (2014) 1681–1698.
[43] P. Sedlák, H. Seiner, M. Landa, V. Novák, P. Šittner, L. Mañosa, Acta Mater. 53 (2005) 3643–3661.
[44] V. Recarte, R.B. Pérez-Sáez, E.H. Bocanegra, M.L. Nó, J. San Juan, Mater. Sci. Eng. A 273–275 (1999) 380–384.
[45] W.G. Liu, M. Zhu, Z.G. Wang, D.Z. Yang, Metall. Trans. A 23 (1992) 2939–2941.
[46] D. Hodgson, M. Wu, R. Biermann, ASM Handbook, Volume 2, Properties and Selection: Nonferrous Alloys and Special-Purpose Materials 1990, pp. 897–902.
[47] R.F. Hamilton, H. Sehitoglu, C. Efstathiou, H.J. Maier, Y. Chumlyakov, X.Y. Zhang, Scr. Mater. 53 (2005) 131–136.
[48] R.F. Hamilton, H. Sehitoglu, C. Efstathiou, H.J. Maier, Y. Chumlyakov, Acta Mater. 54 (2006) 587–599.
[49] H.E. Karaca, I. Karaman, Y.I. Chumlyakov, D.C. Lagoudas, X. Zhang, Scr. Mater. 51 (2004) 261–266.
[50] Y.I. Chumlyakov, I.V. Kireeva, I. Karaman, E.Y. Panchenko, E.G. Zakharova, A.V. Tverskov, A.V. Ovsyannikov, K.M. Nazarov, V.A. Kirillov, Russ. Phys. J. 47 (2004) 893–911.
[51] Y. Li, Y. Xin, L. Chai, Y.Q. Ma, H.B. Xu, Acta Mater. 58 (2010) 3655–3663.
[52] C. Efstathiou, H. Sehitoglu, A.J.W. Johnson, R.F. Hamilton, H.J. Maier, Y. Chumlyakov, Scr. Mater. 51 (2004) 979–985.
[53] R.D. Dar, Y. Chen, Acta Mater. 91 (2015) 112–127.
[54] S. Zeller, J. Gnauk, Mater. Sci. Eng. A 481–482 (2008) 562–566.
[55] H. Sakamoto, Y. Kijima, Trans. Jpn. Inst. Metals 23 (1982) 585–594.
[56] S. Miyazaki, K. Otsuka, H. Sakamoto, K. Shimizu, Trans. Jpn. Inst. Metals 22 (1981) 244–252.
[57] P. Zhang, A. Ma, S. Lu, G. Liu, P. Lin, J. Jiang, C. Chu, Mater. Des. 32 (2011) 348–352.
[58] J. Liu, J.G. Li, Mater. Sci. Eng. A 454 (2007) 423–432.
[59] Y. Ma, S. Yang, W. Jin, X. Liu, J. Alloys Compd. 471 (2009) 570–574.
[60] Y. Ma, S. Yang, Y. Liu, X. Liu, Acta Mater. 57 (2009) 3232–3241.
[61] S. Yang, Y. Liu, C. Wang, Y. Lu, J. Wang, Z. Shi, X. Liu, J. Alloys Compd. 619 (2015) 498–504.
[62] N.P. Laboratory, http://resource.npl.co.uk/mtdata/phdiagrams/alco.htm, 2010.
[63] X. Zhao, M. Qi, D. Yang, J. Mater. Sci. Technol. 6 (1990) 427–430.
[64] Alloy Phase Diagrams, ASM International, 1992.